Bachelorarbeit in Physik

Sebastian Krämer

η' photoproduction at threshold at the BGOOD-Experiment

angefertigt am
Physikalischen Institut

vorgelegt der
Mathematisch-Naturwissenschaftlichen Fakultät

der
Rheinischen Friedrich-Wilhelms-Universität Bonn

April 2024
betreut von Prof. Dr. Hartmut Schmieden

Acknowledgements

I would like to thank Prof. Dr. Harmut Schmieden for giving me this opportunity. My thanks also goes to Dr. Tom C. Jude, Dr. Katrin Kohl and all members of the BGOOD collaboration, who provided great support and help during my work.

Contents

CHAPTER 1

Introduction

Investigating meson photoproduction makes it possible to analyze resonance structures, which give valuable insight into the fundamental interactions at small scales. There are many observables that can be investigated, the beam asymmetry being one of them. For $\gamma p \rightarrow \eta' p$, the beam asymmetry was measured by the GRAAL[1] collaboration in 2015. Their result shows an unexpected structure within a very small energy range directly at threshold (Sandri et al., 2015). Theoretical calculations by EtaMAID (Tiator et al., 2018) and Bonn-Gatchina (Anisovich et al., 2018) show that this may be caused by a resonance with a width on the order of only a few MeV. A width this narrow is very unusual, indicating an exotic structure. To date, this experimental result has not been verified. Since close to threshold, both final state particles move at small polar angles in the lab frame, the BGOOD experiment provides a unique setup for this task. Its high-resolution Forward Spectrometer allows for excellent identification and measurement of the recoil proton at forward angles. Within previous analysis at BGOOD, the process was examined with different levels of exclusiveness in the η' reconstruction. Close to threshold, it showed insufficient resolution in the centre-of-mass polar angle of the fully inclusively reconstructed η' momentum (Alef, 2022). The fully inclusive reconstruction would be particularly interesting for potential future beam-asymmetry analyses because it achieves low statistical errors. With a more accurate measurement of both the recoil proton momentum and the photon beam energy, the inclusive η' reconstruction can be improved today. In this thesis, the centre-of-mass polar angle resolution close to threshold is re-examined with the improved measurement methods.
In Chapter 2, the motivation for further analyzing the results of the GRAAL measurement is laid out in more detail, together with the relevant physical context. Chapter 3 focuses on the BGOOD experimental setup and the most important analysis tools governing this analysis. Chapter 4 contains the analysis itself, while all results are concluded and combined with perspectives on the future analysis of η' photoproduction in Chapter 5.

[1] *Grenoble Anneau Accelerateur Laser*, Engl. Grenoble Laser Accelerator Ring

CHAPTER 2

Motivation and Physical Context

This chapter will explain the physical motivation behind this work more precisely. This includes, in particular, the GRAAL measurement and its implications and the results of previous analysis at the BGOOD experiment in this regard. Furthermore, the relevant kinematic properties of photoproduction processes close to threshold are presented.

2.1 Indications for a tiny resonance close to the η' photoproduction threshold

As mentioned, the key observation of interest that led to this analysis goes back to the first measurement of the beam asymmetry Σ for η' photoproduction off the proton, published by GRAAL back in 2015 (Sandri et al., 2015). Examining the beam asymmetry of a scattering process can give valuable insight into the spin-dependency of interactions and thus lead to revelations about the underlying hadronic structure. It is defined by the following ratio of cross-section sums

$$\Sigma = \frac{\sigma_+ - \sigma_-}{\sigma_+ + \sigma_-},$$

where σ_+ and σ_- represent the cross-sections for fully polarized beams in opposite directions.
The experimental result for the beam asymmetry of $\gamma p \rightarrow \eta' p$ close to threshold can be seen in Figure 2.1. One observes a structure unusual for several reasons (Tiator et al., 2018). Not only does the angular distribution show a sinus-type shape, but there is also an extraordinarily high energy dependence. The structure almost disappears within changes of only a few MeV in the centre-of-mass energy W. Updated theoretical calculations accounting for the Σ measurement data were made by EtaMAID (Tiator et al., 2018) and the Bonn-Gatchina Partial Wave Analysis group (Anisovich et al., 2018). Although using different partial waves for their models, both show improved fits when including a tiny resonance ($\Gamma < 3\,\text{MeV}$) roughly at 1 900 MeV.
The suggested narrow width differs from those of many known resonances like the Δ-resonance by one to two orders of magnitude (Workman et al., 2023). This makes the GRAAL result and its implications particularly interesting, as they indicate that the underlying structures might be of an exotic nature, exceeding the classical constituent quark model. Currently, there is little possibility of further inspecting this obscure behaviour. The experimental setup at BGOOD (explained in detail in Chapter 3) is one of

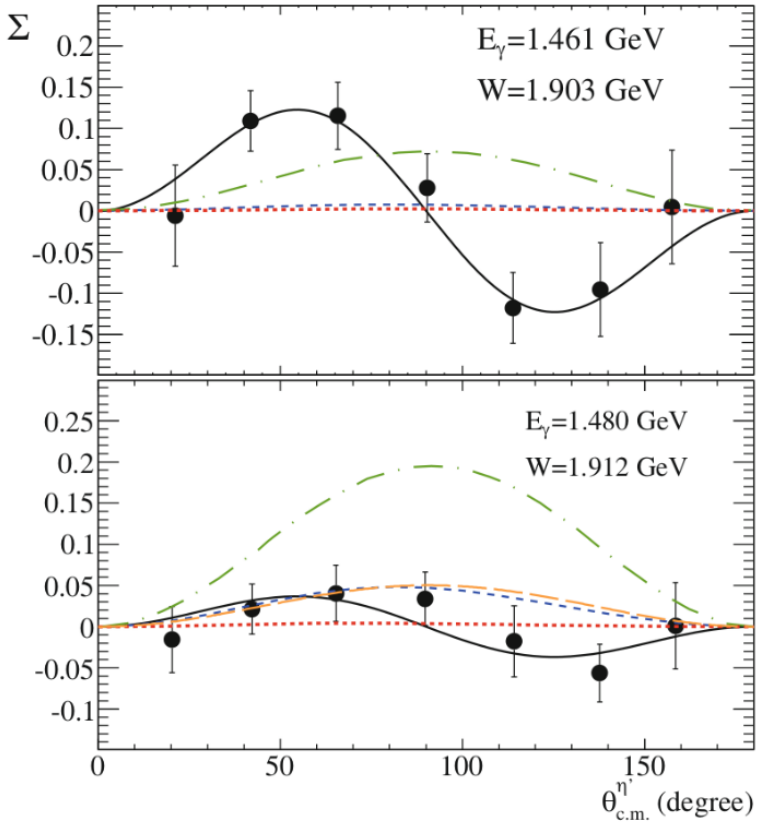

Figure 2.1: GRAAL Measurement of the beam asymmetry Σ of $\gamma p \rightarrow \eta' p$ close to threshold as a function of the meson production angle $\theta^{\eta'}_{c.m.}$ in the CM frame in comparison to different theoretical calculations: red dotted line (Chiang et al., 2003), blue dashed line (Huang et al., 2013) green dot-dashed (Tryasuchev, 2013) and orange long-dashed (Zhong and Q.Zhao, 2011). Figure taken from (Sandri et al., 2015).

few experiments worldwide that might be able to investigate this finding further. A study evaluating this possibility was published in 2022 (Alef, 2022).

2.2 Prior studies of η' photoproduction off the proton at BGOOD

The mentioned study investigated how to use the BGOOD experiment to re-examine the GRAAL beam asymmetry results (Alef, 2022). Different reconstruction methods for the η' 4-momentum were used. Reconstructing it from 4-momentum conservation, as the difference between the respective momenta of the initial state and the recoil proton, was named the *inclusive* reconstruction method. It was compared to more *exclusive* reconstructions in which additional requirements on detected η' decay products were made. Without these additional requirements, the background is significantly increased, as detecting the recoil proton alone does not imply that it must have been produced in the reaction $\gamma p \rightarrow \eta' p$. Therefore, many reactions contribute to the background. On the other hand, less restrictive assumptions are required for inclusive reconstruction. Thus, one benefits from strongly increased statistics. In fact, the previous

analysis found that only the inclusive reconstruction could reduce the statistical error sufficiently to distinguish between the EtaMAID parametrizations, with or without the narrow resonance. However, it was also shown that the centre-of-mass (CM) angle resolution in the energy bin closest to threshold at the time only allowed for separating into two bins over the full range $(-1, 1)$. This limits the precision of cross-section measurements in $\cos\theta^{\mathrm{CM}}$ and the ability to compare a potential beam asymmetry measurement with the nodal structure measured by the GRAAL collaboration. If a higher angular resolution could be achieved, it would ideally be possible to see an η' peak in the energy spectrum for each angular bin. The high background could be modelled with a fit and thus be subtracted. This would be a major advantage compared to GRAAL, where it was impossible to characterize the background.
In order to understand the difficulties associated with accurately reconstructing the CM polar angle and how to improve the resolution, the kinematics of the photoproduction process close to threshold need to be understood.

2.3 The photoproduction process and its kinematics

The Feynman diagram for the process $\gamma p \rightarrow \eta' p$ can be seen in Figure 2.2. Intermediate states can be realized by baryonic resonances. This includes the narrow resonance mentioned in 2.1, assuming it exists.

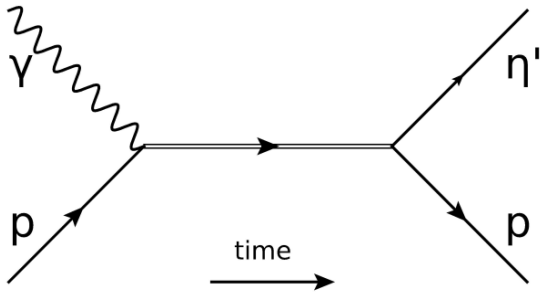

Figure 2.2: Feynman diagram of the photoproduction process, where a real photon interacts with a proton to form an η' meson and a proton. A possible intermediate state is indicated by a double line. Figure taken from (Alef, 2022).

Note that the threshold of this reaction is located at a CM energy W of

$$W^{\mathrm{th}} = m_p + m_{\eta'} \approx 1\,896.95\,\mathrm{MeV}, \tag{2.1}$$

where the masses $m_p \approx 938.27\,\mathrm{MeV}$ and $m_{\eta'} = 957.78\,\mathrm{MeV}$ were used (Workman et al., 2023). Near threshold, energy and momentum conservation strongly restrict the individual transverse momenta of the final-state particles in the lab frame. Hence, all final-state particles are guaranteed to move within a small cone surrounding the beam axis. This implies that a large range of polar angles in the CM frame is boosted into a small range of polar angles in the lab frame. Therefore, by detecting the proton in forward directions, wide CM angular ranges can be studied. The drawback is that small inaccuracies in measuring forward particles increase massively when boosting to the CM frame. For constructing the η'

inclusively, the reconstructed CM angle[1] is a function of the momentum magnitude p_p of the recoil proton, its polar angle θ_p and the beam energy E_b. The resolutions of these quantities must be increased to improve the overall resolution of the CM angle for a given energy bin.

2.4 Aim of this Work

As indicated, refining the beam energy and recoil proton momentum measurements could improve the resolution in $\cos\theta^{\mathrm{CM}}$ close to threshold. It might set the path for a future beam asymmetry measurement. This work examines the effects of using the higher-resolution energy detector ARGUS and an alternate momentum determination in the Forward Spectrometer. Based on this, recommendations are given on how to follow up the investigation of the GRAAL result with the BGOOD setup.

[1] *The* CM angle in this work always refers to the polar angle of the η' meson in the CM frame.

CHAPTER 3

Experimental Setup and analysis tools

The BGOOD experiment is a fixed-target experiment located at the Electron Stretcher Anlage (ELSA) at the University of Bonn. It consists of multiple detectors used to achieve and analyze meson photoproduction. This chapter presents the individual detectors, their performance, and the essential analysis tools used to perform this work.

3.1 BGOOD Experimental Setup

Figure 3.1 schematically shows the detectors' arrangement at BGOOD. The information presented in this chapter is taken from (S.Alef et al., 2020).

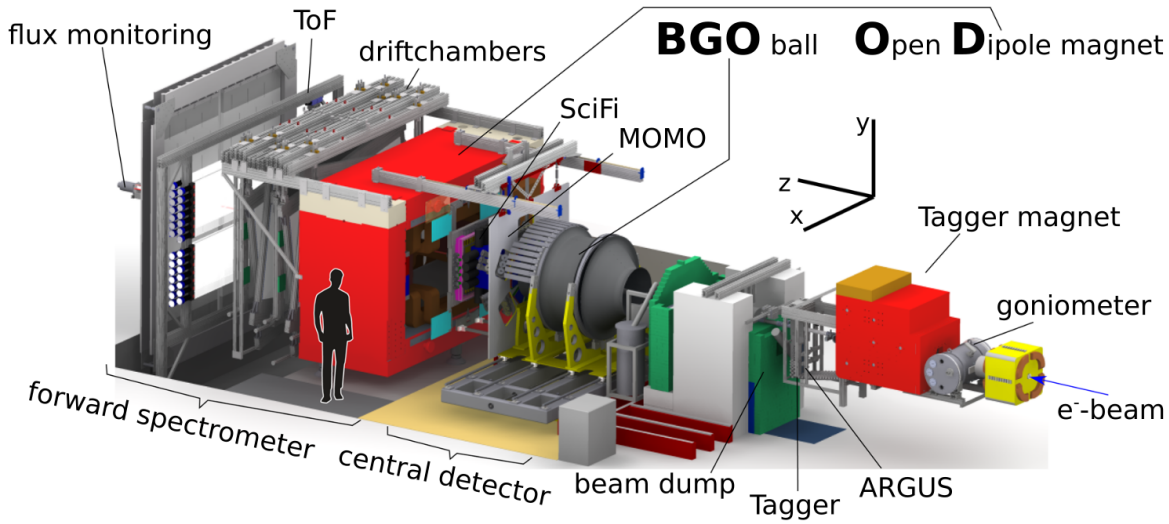

Figure 3.1: Schematic Illustration of the Setup at BGOOD. The electron beam is provided by ELSA. Figure taken from (S.Alef et al., 2020).

3.1.1 The electron beam from ELSA

The electron stretcher facility ELSA at the University of Bonn is a three-stage electron accelerator. Its setup is shown in Figure 3.2. Electrons used within ELSA are obtained either by using a thermal gun

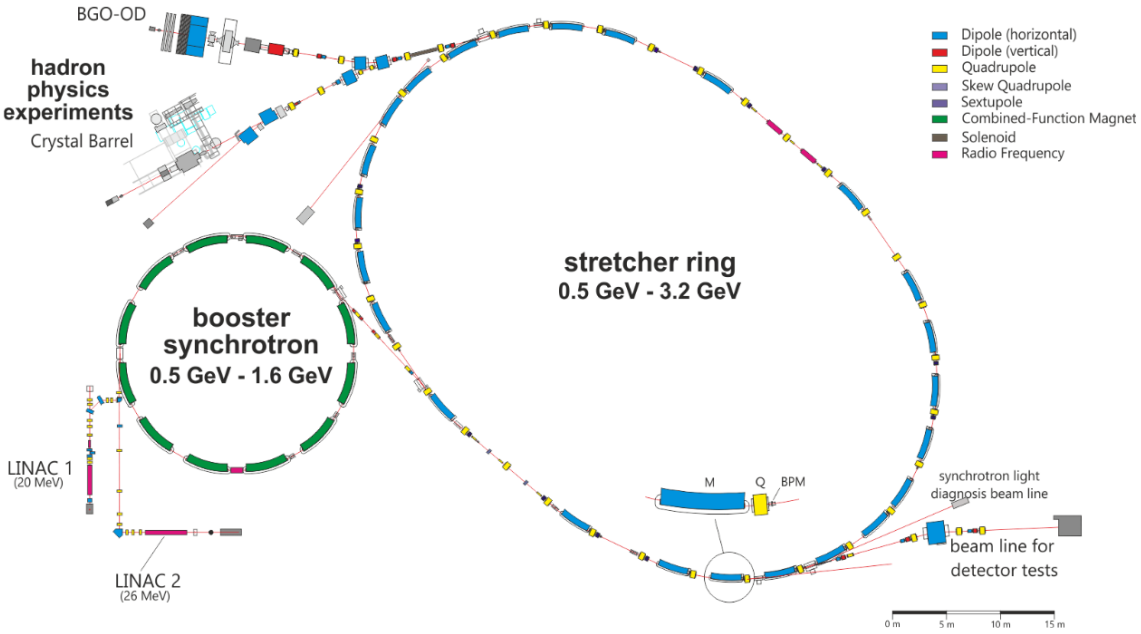

Figure 3.2: Setup of the electron accelerator ELSA at University of Bonn. Figure taken from (Hillert et al., 2017).

to release them from a cathode or through a source of spin-polarized electrons. In the first stage, the linear accelerator *LINAC2*, the previously obtained electrons are boosted to an energy of up to 26 MeV, after which they are transferred to the second stage. Within this booster synchrotron, electrons reach energies of up to 1.6 GeV. Upon reaching the maximum energy, the electrons are transferred to the third and final stage, the stretcher ring. A homogenous filling of the stretcher ring is achieved through multiple injections from the booster synchrotron before the final acceleration to the desired energy (max. 3.2 GeV) takes place. The final electron beam is then extracted to either one of the two hadron physics experiments on-site, Crystal Barrel or BGOOD, or used for detector tests. When used at BGOOD, the accelerated electron beam is first directed onto the radiator in the tagging system.

3.1.2 Tagging System

After being directed to the BGOOD experiment, the ELSA electron beam is converted into a photon beam. Simultaneously, its energy is measured. This happens in the photon tagger. Figure 3.3 depicts a conceptual side view. It consists of a radiator, a dipole magnet and the hodoscope, a combination of 120 scintillator bars. ELSA's electrons with individual incident energy E_0 are directed towards the thin radiator (few hundred µm), where they produce bremsstrahlung photons. A goniometer system allows for a choice of different radiators. This includes copper radiators to produce unpolarized photons and diamond radiators to produce linearly polarized photons. Moving forward along the beam path, the photons and electrons pass a dipole magnet. Due to the Lorentz-Force, electrons are deflected in

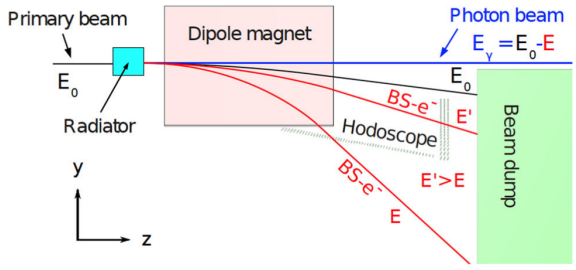

Figure 3.3: Schematic representation of the photon tagger functioning. Figure taken from (S.Alef et al., 2020).

this magnetic field, while the photons' motion remains unaffected. The extent to which an individual electron's trajectory is bent depends on its energy E: lower-energy electrons are deflected stronger than ones with higher energy.
Because of this, the electron's energy can be determined from the detection position within the hodoscope. Should an electron not undergo bremsstrahlung, it will have too much energy to hit the hodoscope and thus land in the beam dump. The latter also holds for electrons that lose too much energy in the bremsstrahlung interaction. A photon must have been produced previously for events where the electron hits the hodoscope. This photon's energy can be calculated using energy conservation:

$$E_\gamma = E_0 - E.$$

This achieves resolutions from 0.55 %E_0 to 2.28 %E_0 (Bella, 2016) in a range from 10 %E_0 to 90 %E_0. For usual energies of the ELSA electron beam (around 2.9 GeV), this corresponds to a binwidth on the order of 30 MeV.

3.1.3 ARGUS

The scintillating fibre detector ARGUS is positioned ahead of the tagger's vertical segment relative to the post-bremsstrahlung electrons' flight path. It consists of 480 fibres and improves the energy resolution of the tagging system. The resolution achieved ranges from 0.08 % to 0.45 % of the electron beam energy (Reitz, 2015), covering a range from 30 % to 66 % of E_0. This results in binwidths on the order of 10 MeV for usual operation.

3.1.4 Central Part

After leaving the tagging system, the post-bremsstrahlung photons reach the central part of the experiment. This consists of the target, two MWPCs[1], a scintillator barrel and the BGO[2] calorimeter. Figure 3.4 shows a slice view of the composition. The beam is directed to meet the target cell in the centre of the BGO calorimeter. The target length and material can be chosen from liquid hydrogen and liquid deuterium. Surrounding the target are two MWPCS, used for charged particle tracking, and a scintillator barrel. The barrel is made from 32 scintillator bars, each 5 millimetres thick. Detection efficiencies differ for charged and neutral particles. This can be used to separate between the two. Surrounding the

[1] Multi-Wire-Proportional-Chambers
[2] Bismuth Germanate

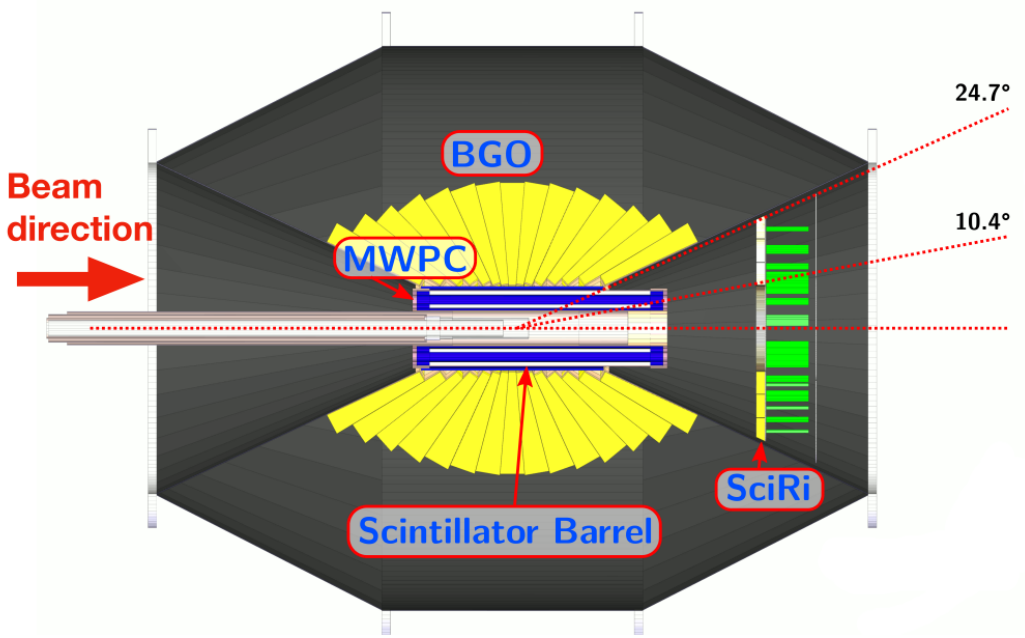

Figure 3.4: Central Part of the BGOOD experiment, consisting of the target, two Multi-Wire-Proportional-Chambers, the BGO Rugby Ball and SciRi. Figure taken from (S.Alef et al., 2020).

target lies the BGO calorimeter. It is partitioned into 15 groups of 32 crystals each, adding up to 480 crystals in total. Photomultipliers and Analog-Digital-Converters are used for signal processing. The covered polar angular range reaches from 25° to 155°. Due to its shape, the calorimeter is also often called the BGO Rugby Ball. It is optimized to detect photons by measuring the electromagnetic showers they induce, but it can also be used to observe charged particles.
The SciRi[3] is used for additional coverage between the central detector and the forward spectrometer (explained in detail in Section 3.1.5). It detects the direction of charged particles.
Since this work focuses on inclusive reconstruction, the detectors in the Central Part were not used for the analysis. They are still included in this setup overview so that its full functionality can be understood.

3.1.5 Forward Spectrometer

The Forward Spectrometer, positioned behind the central detector concerning the beam propagation direction, precisely identifies charged particles in forward directions and measures their 3-momentum and velocity β. It operates in an approximate polar angular range from 1.5° to 12°. The spectrometer consists of a large Open Dipole Magnet (OD Magnet) that deflects charged particles in combination with scintillation detectors SciFi2 and MOMO for front tracking and drift chambers for rear tracking as well as a ToF[4] Spectrometer. Figure 3.5 shows a top view of the arrangements of the mentioned detectors.
A charged particle entering the forward part of the Forward Spectrometer first crosses the scintillating fibre detectors MOMO and SciFi2. MOMO contains three layers and a total of 672 fibres. The layers each have a relative angle of 60° to one another. SciFi2 constitutes another 640 fibres, separated into two

[3] Scintillating Ring detector
[4] Time-of-Flight

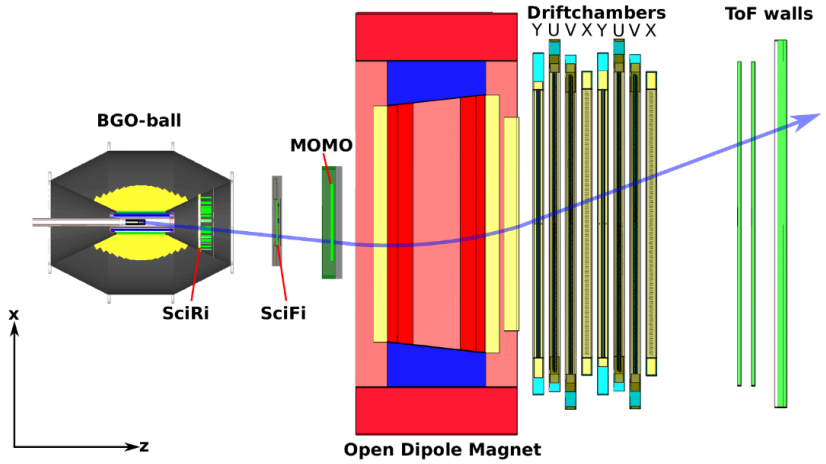

Figure 3.5: Top view of the charged particle trajectory within the different parts of the Forward Spectrometer. Capital Letters U, V, X and Y represent different drift chamber orientations. Figure adapted from (Schleuchin, 2019).

orthogonal layers. In combination, MOMO and SciFi2 track particles before entering the Open Dipole Magnet field. Within the Open Dipole Magnet, which reaches fields of up to 0.4 T, charged particles are subject to the Lorentz Force. Because of that, their trajectories are bent according to their charge and momentum. Eight tungsten drift chambers are used to track the effect of the Lorentz deflection behind the OD magnet. The chambers are arranged in four orientations, removing ambiguities in track finding. In Figure 3.5, these orientations are labelled using X (vertical), Y (horizontal), U (vertical, tilted by 9°) and V (vertical, tilted by -9°). The chambers are filled with a mixture of carbon dioxide and Argon. A position resolution of roughly 300 µm is achieved.
The charged particle's path can be reconstructed using its detection positions before and after passing the magnet. From the path's curvature, the momentum can be measured. At the end of the Forward Spectrometer, three time-of-flight (ToF) walls are placed. Horizontal scintillating bars determine the flight time and thus the velocity β. As the mass of a particle can be determined from its momentum and β using

$$m = \sqrt{\left(\frac{p}{\beta}\right)^2 - \beta^2}, \tag{3.1}$$

particles can be identifed. Figure 3.6 shows a two-dimensional histogram, where the reconstructed β and momentum are marked for every constructed final forward track. For reconstructed momenta below (1.0 to 1.2) GeV, one can see four distinct shapes that align with the theoretical expectation for Pions, Kaons, protons and deuterons, shown as bright lines.
The performance of the Forward spectrometer is essential for the inclusive reconstruction in meson photoproduction. An angular resolution of 0.3° is achieved, and a relative momentum resolution of 3 % when the OD magnet is operated at its full field strength. Yet, at maximum strength, the field of the OD is so strong that many charged particles are deflected to an extent where they can not further be detected. Because of that, the OD magnet usually only operates at half that strength. It will be seen in 4.3.1 that this worsens the relative momentum resolution roughly to 6 %.

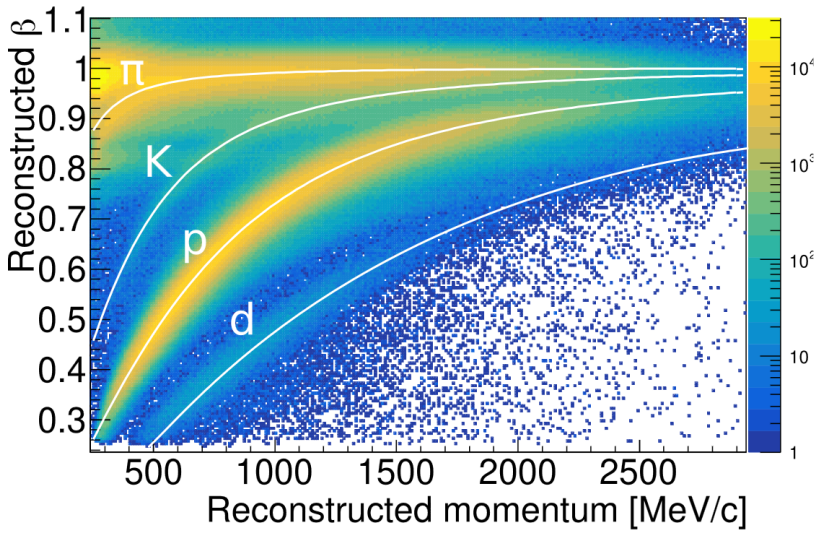

Figure 3.6: Relation between reconstructed β and reconstructed momentum used to identify particles. Figure taken from (Figueiredo, 2023).

3.1.6 Photon Flux Measurements

All parts of the Forward Spectrometer let particles transmit in the very centre. This allows for measuring the photon flux at the very back of the experiment using the Flux Monitor (FluMo) and the Gamma Intensity Monitor (GIM). The lead glass detector GIM is fully absorbent of beam photons. FluMo is used for high beam currents and is calibrated using GIM at lower beam currents. The measurement of the photon flux is essential to achieve normalization in cross-section measurements, which is not part of the analysis performed in this work.

3.2 Analysis Tools

The most important analysis tools used for this work are introduced briefly. These include the C++ library ROOT and the framework ExPlORA, which were used to simulate reactions at the BGOOD setup and process detector signal data.

3.2.1 ROOT

ROOT (Brun and Rademakers, 1997) is a C++ library, that was developed at CERN[5] and is used to process large quantities of data in high-energy physics. It provides a useful structure for physical calculations like performing Lorentz boosts or calculating angles from a given 4-vector.

[5] *Conseil européen pour la recherche nucléaire*, engl. European Organization for Nuclear Research

3.2.2 ExPlORA

ExPlORA[6] is a framework based on ROOT. The full BGOOD experimental setup is implemented in ExPlORA, so reactions and their detection can be simulated. An event generator creates a first instance of the bremsstrahlung photon and all final-state particles before decay. Through Monte Carlo methods, the particle decays and energy depositions in each detector are simulated, including the use of Geant4[7] for particle passage through the material.
ExPlORA can additionally be used to process real and simulated data. In the first step, *hit* objects are created if the signal exceeds a pre-defined threshold. Before physical analysis is performed, the hits of multiple detectors are processed further. Hits within the same detector obeying spatial and time correlation are grouped into a *cluster*. Multiple clusters of different detectors are combined to give a *track*, which is a model for the path taken by a particle. Figure 3.7 illustrates these different objects' relationships.

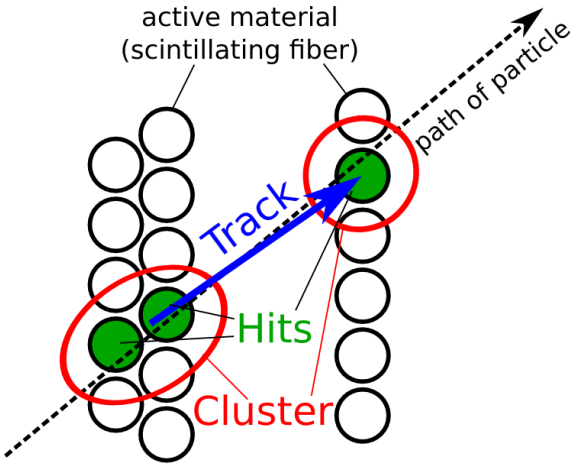

Figure 3.7: Schematic representation of the creation of a track (blue) from multiple clusters (red), each made up of individual hits (green). Figure adapted from (Schleuchin, 2019).

All analyses shown in this work were performed using ROOT and ExPlORA.

[6] Expendable Pluggable Objectoriented ROOT-ified Analysis
[7] Geometry and Tracking 4

CHAPTER 4

Analysis

With the described setup and analysis tools, the analysis can be performed. First, calculations are conducted to examine how individual lab frame resolutions impact the reconstructed polar angle for fixed energies. A method is shown to quantify this impact and assign a resolution for each chosen lab frame resolution. From this, the distinct influences of uncertainties in single observables are combined to give an overall resolution. Both measurement refinement methods mentioned are analyzed with respect to their effect on this overall resolution. Comparisons are made to the resolutions achieved by GRAAL.

4.1 Angular resolution effects from single observables

When reconstructing the η' momentum inclusively, the lab frame quantities E_b, θ_p and p_p determine the value of the reconstructed CM angle θ^{CM}. Since values of all these quantities can only be measured with a finite accuracy in a real experiment, each one contributes to the overall resolution in θ^{CM}. To understand the limitations in the θ^{CM} reconstruction close to threshold, it is instructive first to establish how contributions of individual observables compare to one another.

4.1.1 Introduction of a resolution measure

To examine the effect of uncertainties in a single observable on the reconstructed θ^{CM}, perfect precision must be achieved for the other two variables. The exact physical values for all three observables are calculated from initial choices for the beam energy and the CM angle to simulate this. A finite resolution in one of the lab frame quantities is imitated by deliberately changing the calculated value using a random distribution. The other two values remain unchanged. The CM polar angle can be recalculated using the altered value. Repeating this many times will yield a distribution in the reconstructed angle. An example of such an obtained distribution is shown in Figure 4.1. It was created by a variation of the proton momentum.
Naturally, the statistical fluctuation of the proton momentum results in statistical fluctuations for the reconstructed angle. The resulting shape is not symmetrical, an artefact of the mathematical relation between the two quantities. The distribution shows a peak-like structure with the peak position being close to the nominal value $\cos\theta^{\mathrm{CM}}_{\mathrm{nom}} \approx -0.77$. The distribution has a mean of -0.74 and a standard deviation of 0.11. The standard deviation indicates how much the values spread away from the mean.

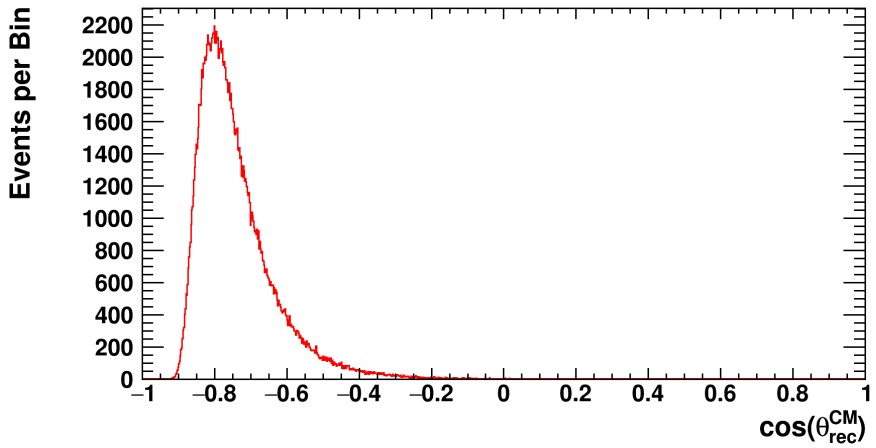

Figure 4.1: Resolution effect on the reconstructed $\cos\theta^{\mathrm{CM}}_{\mathrm{rec}}$ from inserting an inaccuracy in the proton momentum magnitude. The inaccuracy was generated using a Normal Distribution centred at the original momentum value with a standard deviation of 25 MeV. This corresponds to a relative momentum resolution of 3 %. The initial values taken for the calculation are $E_b = 1\,460\,\mathrm{MeV}$ and $\theta^{\mathrm{CM}}_{\mathrm{nom}} = 140^\circ$ ($\cos\theta^{\mathrm{CM}}_{\mathrm{nom}} \approx -0.77$).

As such, it can be used here as a rough measure for the resolution of θ^{CM} that results from the finite resolution of the proton momentum. Analogously, the beam energy and proton polar angle can be varied. Using the standard deviation as a resolution measure for the variation of each observable provides a way to compare their different contributions to the overall resolution.

Before comparing the different CM angle resolution contributions, the question arises of how the statistical fluctuations should be performed to best model the inaccuracies introduced by real measurements. Ultimately, this means choosing the random distributions used to sample the altered values. For the beam energy E_b, the energy distribution roughly follows a $1/E_b$ shape due to the bremsstrahlung origin of the photons. For intervals of a width around 30 MeV at energies around 1 GeV, this can be approximated to be constant. Because this is practically achieved (see Section 3.1.2), a Uniform distribution of width ΔE is used to model beam energy measurements. Measurements of both proton angle and proton momentum are modelled straight-forwardly using Gaussian distributions. As established in Chapter 3.1.5, the proton momentum resolution for the real setup depends on the momentum approximately linearly. Because of this, the modelled Gaussian is chosen to have a standard deviation σ_p proportional to the initial momentum value. The proportionality constant $\epsilon_p = \sigma_p/p$ can be understood as the relative momentum resolution. A list of all mentioned random distributions used to alter the values of lab frame observables can be found in Table 6.1.

This approach can quantify and compare contributions to the CM polar angle resolution by individual lab frame inaccuracies.

4.1.2 Comparing contributions of each observable

For each lab frame observable E_b, p_p and θ_p the just described method is applied for different lab frame resolution parameters ΔE, ϵ_p and σ_θ and different fixed initial values for the *kinematic variables* E_b and

θ^{CM}. Figure 4.2 shows the resulting $\cos\theta^{\mathrm{CM}}_{\mathrm{rec}}$ resolutions.

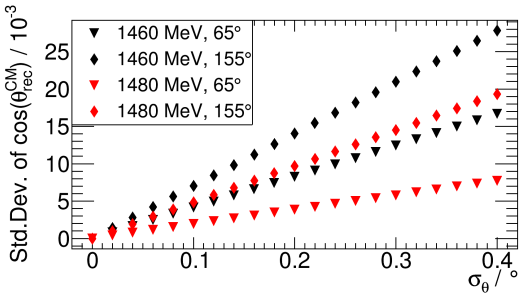

(a) Effects caused by variations in the proton angle θ_p.

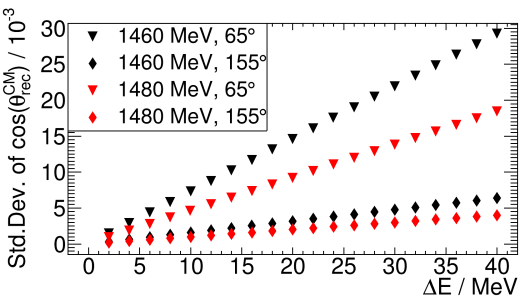

(b) Effects caused by variations in the beam energy E_b.

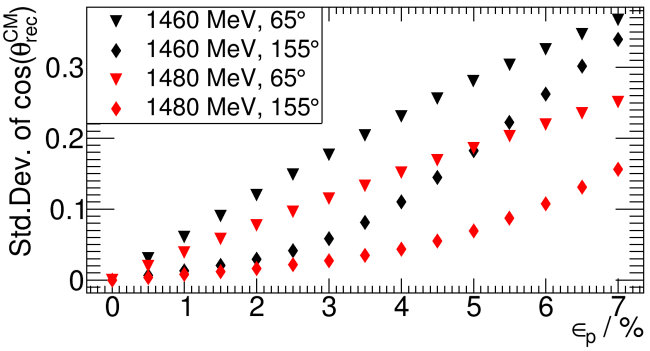

(c) Effects caused by variations in the proton momentum p_p.

Figure 4.2: Effects of resolutions in single lab frame quantities on the CM angular resolution. The latter is characterized by the standard deviation of the respective $\cos\theta^{\mathrm{CM}}_{\mathrm{rec}}$ distribution, which is plotted on the y-axis. For every subfigure, the tampered lab frame quantity differs. The values on the x-axes characterize the introduced lab frame resolutions. In each subfigure, there are four different combinations for the nominal kinematic values E_b (given in MeV) and $\theta^{\mathrm{CM}}_{\mathrm{nom}}$ (given in °).

In Chapter 3, the resolutions for the real setup were stated, which correspond to $\sigma_\theta = 0.3°$, $E_b = 30\,\mathrm{MeV}$ and $p_p = 6\,\%$. This assumes a beam energy measurement using the tagger and an operation of the OD magnet at half its maximum field strength. Comparing the scales of the resulting standard deviations for these values shows that the momentum resolution appears to have the most substantial effect, regardless of the chosen pair of kinematic values. Therefore, improving the proton momentum resolution is most effective in optimizing the CM polar angle resolution close to threshold. Yet, the effect of using ARGUS for beam energy measurements on the overall angular resolution when including all uncertainties needs to be analyzed in more detail.

4.2 Refinement of Beam Energy Measurements using ARGUS

Having estimated the individual resolution contributions of E_b, p_p and θ_p, the effects can now be combined to give a total CM angle resolution. To achieve this, an analogous approach to the one described in Section 4.1.1 can be performed. Modifying all of the calculated quantities E_b, p_p, and θ_p simultaneously rather than only one at a time allows an overall effect on the reconstructed CM angle to be

studied. It is again characterized by the standard deviation of $\cos\theta_{\mathrm{rec}}^{\mathrm{CM}}$. Figure 4.3 shows the resolutions for $\sigma_\theta = 0.3^\circ$ and $\epsilon_p = 6\,\%$. The energy resolutions were chosen to be 30 MeV and 10 MeV to represent the Tagger and ARGUS respectively.

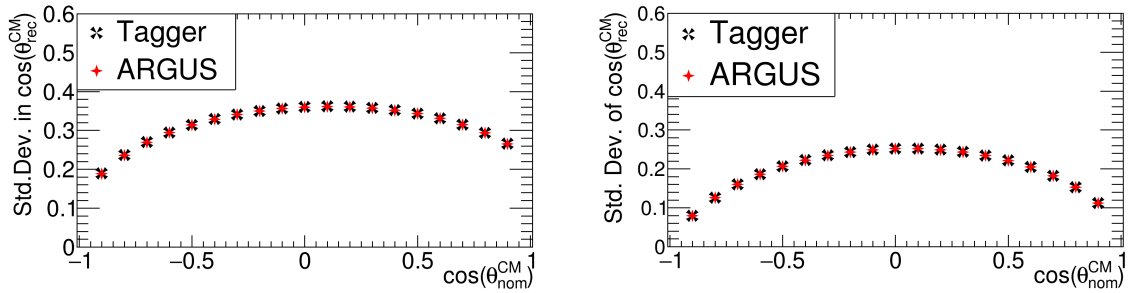

(a) $E_b = 1\,460$ MeV (b) $E_b = 1\,480$ MeV

Figure 4.3: Comparing angular resolutions for Tagger and ARGUS at two energies near threshold. The standard deviation of the polar angle distribution again characterizes the angular resolution.

For both considered energies, it is not possible to distinguish between using ARGUS or the Tagger. What was proposed at the end of Section 4.1.2 is reassured: the momentum resolution is the limiting factor for the polar reconstruction. Even more, the energy resolution appears to have a negligible impact. The momentum resolution needs to be improved to improve the CM polar resolution close to threshold significantly.

4.3 Refinement of Proton Momentum Measurements

While, in principle, it would be possible to refine proton momentum measurements by changing the OD field strength to its maximum value, there are side effects (see Section 3.1.5). This option is undesirable as low-momentum particles are lost and the available statistics decrease. Even so, there is another way to improve the momentum resolution.
As stated in 3.1.5, the Forward Spectrometer is used to identify particles by measuring their momentum and velocity β and calculate the mass via 3.1. The determined mass will generally differ from the nominal mass of the particle. After identifying the particle from the velocity and the momentum, one can recalculate the momentum from the nominal mass and β. The high time resolution in the ToF spectrometer can improve momentum resolution, depending on the particle. For protons, this has not yet been analyzed. To separate between the two described methods, the following terminology is introduced: The conventional method to obtain the momentum directly from the track curvature will be called the *TC*-method, and the alternate method that uses β and the nominal mass after identification will be called the β-method.

4.3.1 Comparing Momentum Reconstruction Methods

To analyze how the TC method and β-method compare, the reaction $\gamma p \to \eta' p$ is simulated via ExPlORA. Only those events that result in a successfully constructed proton forward track are considered. This track extracts either the TC-momentum or the β-momentum as a measurement p_{meas}. Other than for real data, in simulation, it is also possible to access the initially generated "true" momentum p_{gen} of the final

state proton. The difference

$$\Delta p = p_{\text{meas}} - p_{\text{gen}}$$

can be regarded as a measurement inaccuracy and can be studied for different generated momentum values. Figure 4.4 compares the momentum measurement error for the two reconstruction methods.

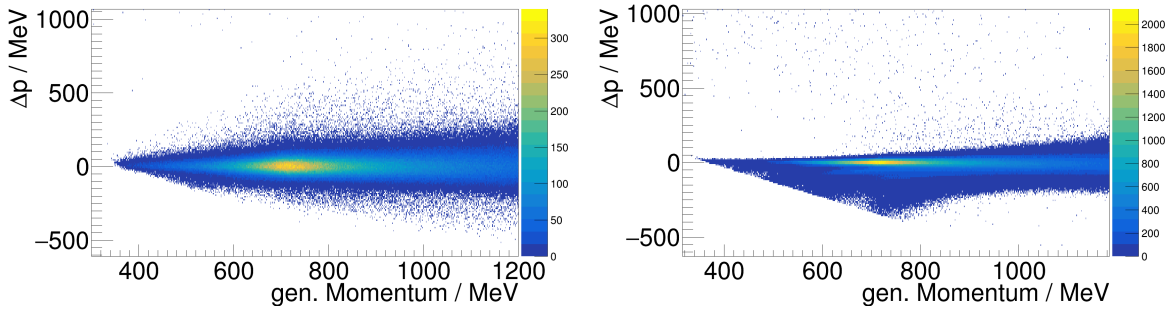

(a) Using TC-momentum as measured momentum

(b) Using β-momentum as measured momentum

Figure 4.4: Proton momentum inaccuracy Δp in an ExpPlORA simulation of $\gamma p \rightarrow \eta' p$. Only events with Forward Tracks identified to belong to protons are considered. Of those, events where the generated momentum exceeded 1.2 GeV were neglected because particle identification would not be possible. The method for measuring momenta is different between the two figures.

One can see that the region most of the events fall into is vertically much narrower for the TC method. This corresponds to a better momentum resolution. It should also be noted that the TC method gives a symmetrical shape, while the recalculated $beta$ momentum tends to be systematically smaller than the generated momentum. This might be due to time calibration in the ToF but is not particularly relevant for this work since the vast majority of β-momenta align excellently with the generated value.
To quantify the resolution improvement, Gaussian curves are fitted to every respective Δp distribution within a fixed p_{gen} bin for both methods. The Gaussian fit curve's standard deviation σ can be seen as a momentum resolution for the respective p_{gen} bin used. Dividing each standard deviation by the corresponding p_{gen} bin-centre results in the dimensionless relative resolution $\epsilon = \sigma / p_{\text{gen}}$. Figure 4.5 shows the relative resolutions for both momentum reconstruction methods.
For the TC method, the relative resolution ϵ is almost constant at a value close to 6 %. This is the result anticipated in 4.1.1. For using the β-method the relative resolution fluctuates more, but lies between 2 % to 4 % for momenta up to 1 GeV, with a mean at 3 %. The Comparison of both graphs shows that the β-method improves the momentum resolution for all simulated momenta. This is a crucial insight, as this has so far only been tested for deuterons (Figueiredo, 2023). Even more, the improvement has been quantified and can be used to determine an updated $\cos\theta^{\text{CM}}$ resolution.

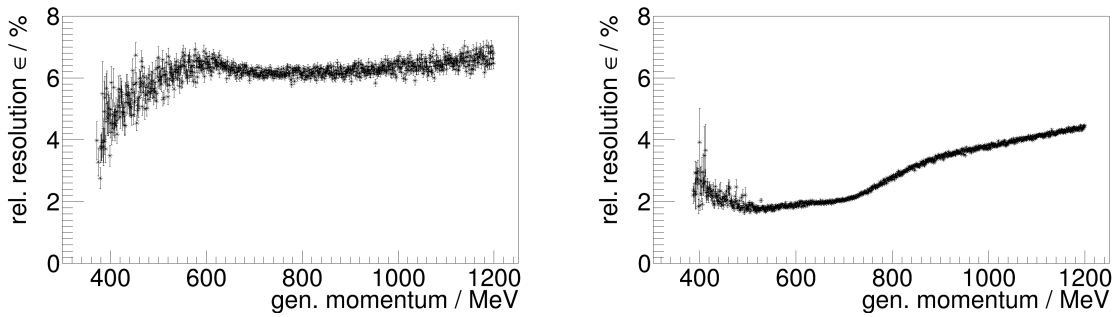

(a) Using TC-momentum as measured momentum

(b) Using β-momentum as measured momentum

Figure 4.5: Relative Momentum Resolution for each momentum bin. In simulation, Gaussian Fits are applied to the Δp distribution within each p_{gen} bin. The relative resolution ϵ is set to equal the standard deviation of the Gaussian Fit Curve divided by the corresponding bin centre momentum. The uncertainty in the x-direction corresponds to half the binwidth, and the one in the y-direction is the uncertainty on the fit parameter σ. TC- and β-methods are compared.

4.3.2 Improved Angular Resolution

As has been established, the momentum resolution has the strongest influence on the CM angle distribution. Having quantified by how much the β-method refines the momentum measurement, the effect on the CM angle reconstruction can be determined. Figure 4.6 shows the standard deviations of the reconstructed $\cos\theta^{\text{CM}}_{\text{rec}}$ distributions for the two momentum reconstruction methods. For the TC method $\epsilon_p = 6\,\%$ is assumed, while $\epsilon_p = 3\,\%$ was used for the β-method.

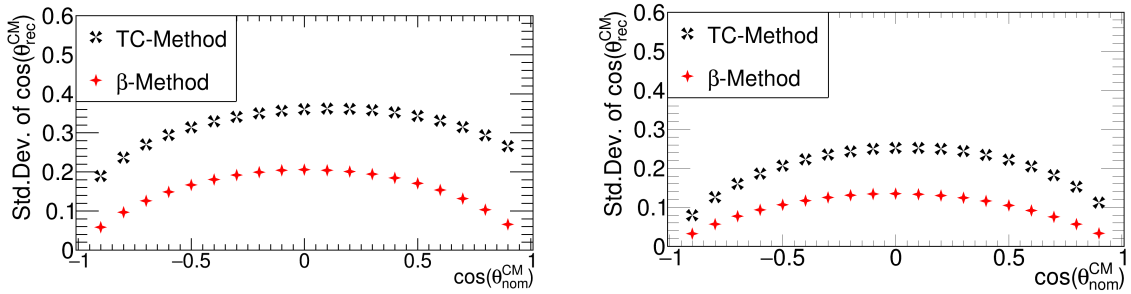

(a) $E_b = 1\,460\,\text{MeV}$

(b) $E_b = 1\,480\,\text{MeV}$

Figure 4.6: Comparing the momentum reconstruction methods concerning the resulting CM angular efficiency. The energy resolution was taken to model the tagger binwidth at 30 MeV and the angular resolution is fixed to 0.3°

When using the β-constructed momentum, a clear improvement can be seen for all angles and both energies analyzed. For the original resolution, it was shown that directly at threshold, data could only be grouped into one forward direction and one backward direction bin (Alef, 2022). When using the β-method, angle distinction is much improved, such that a much finer binning could be achieved. Because the ultimate goal is verifying or falsifying the GRAAl result, it stands to reason to check whether the BGOOD setup with the improved resolution can reproduce their binning.

4.4 Reproducing the GRAAL binning at BGOOD

Figure 2.1 shows that at divided the data was divided into seven evenly spaced angular bins. For the higher energy (1 480 MeV), a division into seven angular bins was already possible with the unimproved resolution (Alef, 2022). This was impossible for the lower energy of 1 461 MeV and can now be re-evaluated.
To do so, for each angle, an interval with a width twice as large as the corresponding angular resolution is drawn and checked for overlap. If the resulting intervals show significant overlap, data cannot reliably be sorted into a unique interval due to uncertainty. Figure 4.7 shows the intervals as error bars, with the data point representing the angle from which the resolution was used. The intervals are placed at alternating y-values to avoid visual cluttering. To better compare this to the original GRAAL binning, the intervals are drawn in terms of θ^{CM} rather than its cosine.

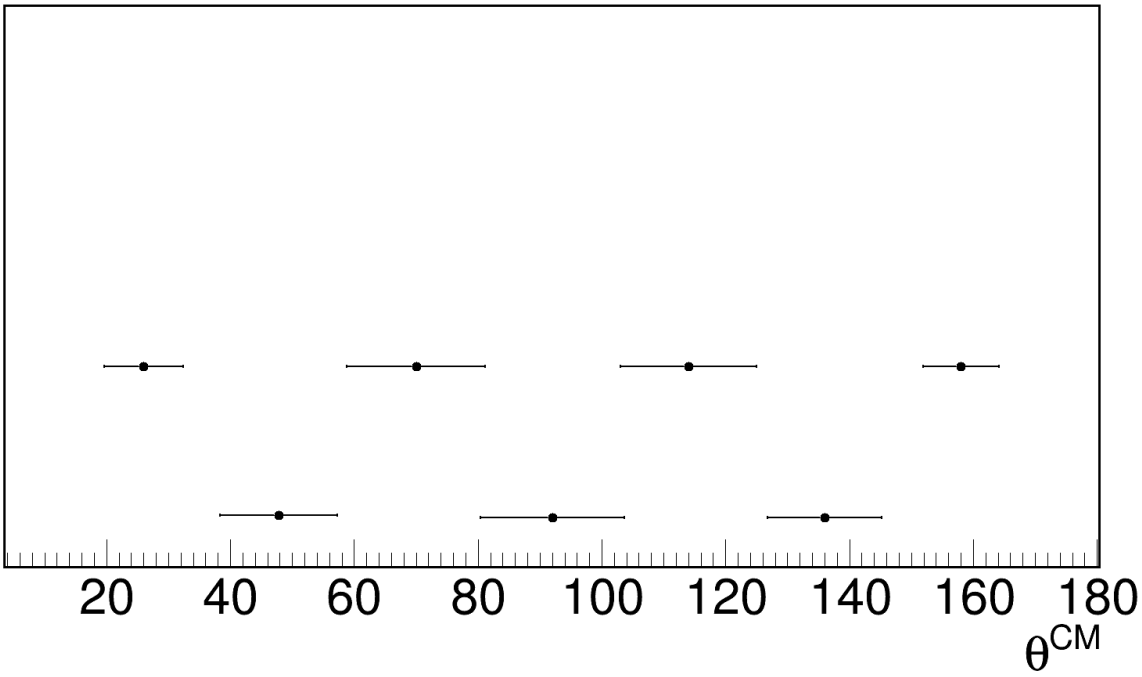

Figure 4.7: Possible binning in θ^{CM} at $E_b = 1\,461$ MeV. The error bars are positioned at different vertical positions to avoid visual cluttering.

With the improved resolution, it can be seen that the resulting intervals do not show significant overlap. This indicates, that data can reasonably be sorted into one of those intervals despite the uncertainty on the angle. Hence, the intervals drawn here may be taken as angular binning, which means that when using the β-method to determine the momentum, the BGOOD setup can reproduce the GRAAL binning. Future analyses at the BGOOD experiment may use this binning further to investigate η' at threshold.

CHAPTER 5

Conclusion of Results and Future Perspectives

It was shown that the momentum resolution in the Forward Spectrometer is the limiting factor for accurate inclusive polar angle reconstructions for the current experimental setup at BGOOD. Concerning this angular resolution, using the scintillating fibre detector ARGUS did not show a notable improvement. A modification of the momentum reconstruction in the Forward Spectrometer showed a significantly higher resolution (2 % to 4 %) than the conventional reconstruction (6 %). This increased performance substantially affected the resolution of the inclusively reconstructed CM polar angle. It was concluded that with the updated angular resolution, the same partitioning of data into angular and energy bins can be achieved as for GRAAL without significant overlap. In a future analysis of the η' photoproduction process, real data can be organized into the new angular binning and inspected for an η' peak in the energy spectrum.

CHAPTER 6

Appendix

Table 6.1 shows the list of Probability Distributions that were used to introduce uncertainties to calculated values. See Chapter 4.1.1 for the detailed description.

Lab Frame Observable	Probability Distribution	Probability Density Function (PDF)
Proton Polar angle θ_p	$\widetilde{\theta}_p \sim \mathcal{N}(\mu = \bar{\theta}_p,\ \sigma = \sigma_\theta)$	$f(\widetilde{\theta}_p) = \frac{1}{\sqrt{2\pi\sigma_\theta^2}} \exp\left(-\frac{(\widetilde{\theta}_p - \bar{\theta}_p)^2}{2\pi\sigma_\theta^2}\right)$
Proton momentum magnitude p_p	$\widetilde{p}_p \sim \mathcal{N}(\mu = \bar{p}_p,\ \sigma = \bar{p}_p\epsilon_p)$	$f(\widetilde{p}_p) = \frac{1}{\sqrt{2\pi\bar{p}_p^2\epsilon_p^2}} \exp\left(-\frac{(\widetilde{p}_p - \bar{p}_p)^2}{2\pi\bar{p}_p^2\epsilon_p^2}\right)$
Beam Energy E_b	$\widetilde{E}_b \sim \text{Unif}(\bar{E}_b - \frac{\Delta E}{2},\ \bar{E}_b + \frac{\Delta E}{2})$	$f(\widetilde{E}_b) = \begin{cases} \frac{1}{\Delta E} & \text{if } \left\lvert\widetilde{E}_b - \bar{E}_b\right\rvert < \frac{\Delta E}{2} \\ 0 & \text{else} \end{cases}$

Table 6.1: Probability Distributions and their PDFs used to simulate measurements. Symbols topped with a "~" represent Random Variables, sampled to imitate a measurement for the respective quantity. Barred symbols represent the true physical values for the corresponding quantity. σ_θ, ϵ_p and ΔE each determine the width of the PDF they appear in and hence characterize the accuracy of the respective "measurement".

References

Alef, Stefan (2022). "Studies of $\eta' p$ photoproduction at the BGOOD experiment". In: bonndoc (cit. on pp. 1, 3, 4, 18, 19).

Anisovich, A.V. et al. (2018). "Proton-η' interactions at threshold". In: PLB 785 (2018) 626–63 (cit. on pp. 1, 2).

Bella, Andreas (2016). "Linearly polarised photon beams at the BGO-OD experiment at ELSA". In: bonndoc (cit. on p. 8).

Brun, Rene and Fons Rademakers (1997). "ROOT — An object oriented data analysis framework". In: NIM A 389 (1997) 81 (cit. on p. 11).

Chiang, W.-T. et al. (2003). "Reggeized model for η and η' photoproduction". In: Phys. Rev. C **68**, 045202 (cit. on p. 3).

Figueiredo, António João Clara (2023). "Coherent $\pi^0\eta$ photoproduction off the deuteron at the BGOOD experiment". In: *Universität Bonn* (cit. on pp. 11, 17).

Hillert, Wolfgang et al. (2017). "Beam and spin dynamics in the fast ramping storage ring ELSA: Concepts and measures to increase beam energy, current and polarization". In: EPJ Web Conf 134 (2017) 05002 (cit. on p. 7).

Huang, F., H. Haberzettl, and K. Nakayama (2013). "Combined analysis of η' production reactions: $\gamma N \to \eta' N$, $NN \to NN\eta'$, and $\pi N \to \eta' N$". In: Phys. Rev. C **87**, 054004 (cit. on p. 3).

Reitz, B-E. (2015). "Construction of an additional hodoscope for the BGO-OD experiment consisting of scintillator fibres (ARGUS) together with simple π^0 analysis". In: Universität Bonn (cit. on p. 8).

S.Alef et al. (2020). "The BGOOD experimental setup at ELSA". In: EPJA 56 (2020) 104 (cit. on pp. 6, 8, 9).

Sandri, P. Levi et al. (2015). "First measurement of the Σ beam asymmetry in η' photoproduction off the proton near threshold". In: EPJ A **51** (2015) 77 (cit. on pp. 1–3).

Schleuchin, Georg (2019). "$\Lambda(1405)$ photoproduction with the BGO-OD experiment". In: bonndoc (cit. on pp. 10, 12).

Tiator, L. et al. (2018). "Eta and etaprime photoproduction on the nucleon with the isobar model EtaMAID2018". In: EPJA 54 (2018) 210 (cit. on pp. 1, 2).

Tryasuchev, V.A. (2013). "η and η' meson photoproduction on nucleons". In: Phys. Part. Nucl. Lett.**10**, 315 (cit. on p. 3).

Workman, R.I. et al. (2023). "Review of Particle Physics". In: Prog. Theor. Exp. Phys. 2022, 083C01 and 2023 update (cit. on pp. 2, 4).

Zhong, X.-H. and Q.Zhao (2011). "η' photoproduction on the nucleon in the quark model". In: Phys. Rev. C **84**, 065204 (cit. on p. 3).

List of Figures

List of Tables